

Controlling assembly and oscillations of elastic membranes with an active fluid

John Berezney,^{1,2,*} Sattvic Ray,^{2,*} Itamar Kolvin,^{3,*} Mark Bowick,^{4,2} Seth Fraden,¹ and Zvonimir Dogic^{2,5}

¹*Department of Physics, Brandeis University, Waltham MA 02454*

²*Department of Physics, University of California at Santa Barbara, Santa Barbara, CA 93106*

³*School of Physics, Georgia Institute of Technology, 837 State St NW, Atlanta, 30332, GA, USA*

⁴*Kavli Institute of Theoretical Physics, University of California at Santa Barbara, Santa Barbara, CA 93106, USA*

⁵*Biomolecular Science and Engineering Program,
University of California at Santa Barbara, Santa Barbara, CA 93106, USA*

We use the chaotic flows generated by a microtubule-based active fluid to assemble self-binding actin filaments into a thin elastic sheets. Starting from a uniformly dispersed state, active flows drive the motion of actin filaments, inducing their bundling and formation of bundle-bundle connections that ultimately generate an elastic network. The emerging network separates from the active fluid to form a thin elastic sheets suspended at the sample midplane. At intermediate times, the active fluid drives large in-plane and out-of-plane deformations of the elastic sheet which are driven by low-energy bending modes. Self-organized sheets eventually exhibit centimeter-sized global spontaneous oscillations and traveling waves, despite being isotropically driven on micron lengths by the active fluid. The active assembly generates diverse network structures which are not easily realizable with conventional paradigms of equilibrium self-assembly and materials processing. Self-organized mechanical sheets pose a challenge for understanding of how a hierarchy of structure, mechanics, and dynamics emerges from a largely structureless initial suspension of active and passive microscopic components.

I. INTRODUCTION

During biological development, intervening layers of complex forms and functions spontaneously emerge from an embryo that seemingly lacks any large-scale structure. Being inherently far from equilibrium, morphogenesis is driven by inscribing patterns of in-plane strains into elastic epithelial sheets, causing them to fold into complex tissues, organs, and entire organisms [1, 2]. Translating such complex yet highly robust self-organizing processes into the realm of materials science presents a largely unexplored opportunity to generate structural and dynamical materials that are not accessible using well-established paradigms of materials processing. Extensive efforts have elucidated general rules of self-assembly, a thermal process wherein structures that minimize free energy spontaneously emerge from a disordered suspension of microscopic particles with well-defined interactions. While capable of generating very intricate structures [3–6], self-assembly suffers from inherent limitations. It requires microscopic constituents that exhibit Brownian motion and often become kinetically trapped in local energy minima when barriers exceed the accessible thermal energy. Self-assembly thus often fails to reach the target structure that minimizes the global free energy [7, 8]. Finally, self-assembly only yields static structures that lack the alluring dynamical features routinely observed in living matter.

Being composed of energy-consuming motile units, active fluids exhibit persistent turbulent-like flows in the absence of any external drive [9–12]. Such flows power

the random motion of embedded passive objects, allowing them to explore space more efficiently than passive Brownian motion [10, 13, 14]. Motivated by these observations [15], we study the self-assembly of fiber networks whose motion is powered by an active fluid. Specifically, we use a microtubule-based active fluid to power dynamics of otherwise passive actin bundles. In the active fluid, adhesive actin bundles move chaotically, colliding with each other, creating permanent connections, and assembling into an elastic network. In the ensuing actively driven self-assembly process, the emerging elastic structures exert feedback on the active drive, creating a cascade of interacting structural and dynamical processes that ultimately yield centimeter-sized thin elastic sheets that exhibit robust large-scale self-shearing oscillations. These experiments demonstrate how materials with complex structure, mechanics, and dynamics emerge from an initially structureless suspension of active and passive components. They provide an initial step towards mimicking biological morphogenesis with synthetic materials.

II. SELF-ORGANIZED ELASTIC SHEETS

We studied a composite system of passive adhesive filaments and an active fluid. The passive system consisted of filamentous actin (F-actin) and crosslinker fascin, which together formed adhesive bundles (Fig. 1F) [16]. The active fluid consisted of microtubules (MTs) bundled with PRC1, kinesin-streptavidin motor clusters (KSA), and caged ATP (Fig. 1G) [10]. These components were loaded into rectangular quasi-2D chambers of typical dimension 4 mm × 18 mm × 0.1 mm. To generate well-defined initial conditions, monomeric actin was polymerized around non-motile MT-PRC1 bundles, forming an

* These authors contributed equally.

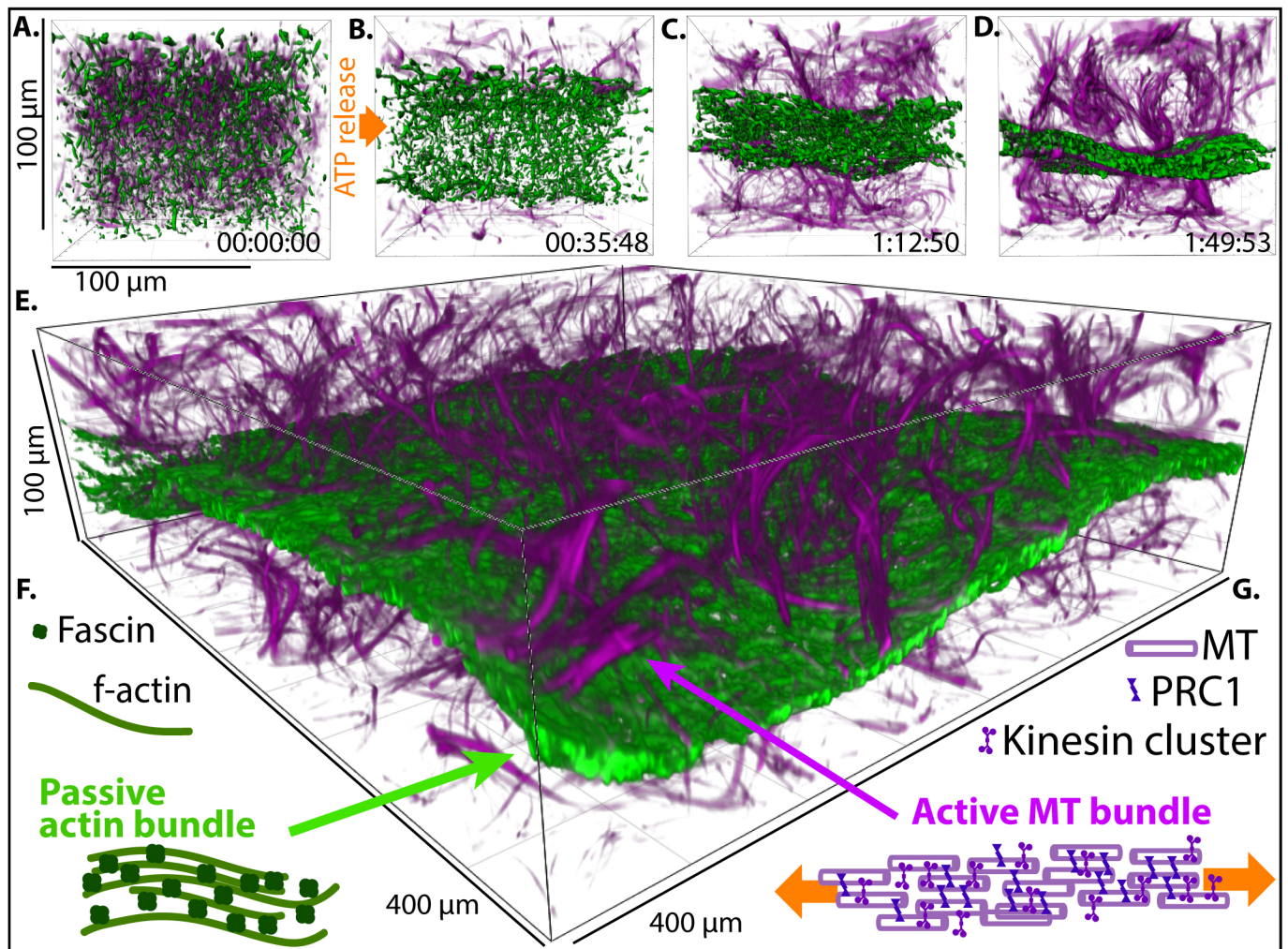


FIG. 1. **Self-organized elastic sheets** (A)-(D) Sequence of rendered 3D confocal images showing active MT bundles (magenta) driving fascin-linked actin bundles (green) into a contracted elastic sheet. (E) Larger view of a section of the actin sheet surrounded by MT bundles. (F) Fascin induces the formation of passive bundles of F-actin. (G) The active fluid consists of filamentous MTs, MT bundler PRC1, and kinesin-streptavidin clusters.

interpenetrating double network (Fig. 1A) [17]. Without activity, these networks were athermal, with structure that remained static over days. The light-induced release of caged ATP initiated stepping of motor clusters along adjacent MTs, causing them to slide relative to each other. The motor-induced sliding drove repeating cycles of MT bundle extension, buckling, fraying, and reformation, generating persistent and autonomous chaotic flows. Lacking specific biochemical interactions, MT and actin only interacted sterically and hydrodynamically. Active flows transported the passive actin bundles, driving their collisions and coarsening over time, eventually forming a percolating elastic network which contracted into a thin sheet suspended at the chamber midplane (Fig. 1B-D,E, Supplementary Video 1). Once in a steady state, the elastic sheet continuously exhibited large in-plane and out-of-plane deformations.

III. DYNAMICS OF SELF-ORGANIZED MEMBRANES

The system outlined exhibited several structural and dynamical states. Before initialization of the active fluid, actin filaments at low fascin concentrations did not form bundles [16]. After activity was induced, actin filaments were fluidized by MT-generated active flows. Initially, both MTs and actin exhibited chaotic flow fields with comparable speeds and highly correlated spatial structure (Fig. 2b,c,d I). During this stage, actin remained unbundled and was uniformly distributed throughout the sample chamber (Fig. 2a,b).

After ~ 2 hours, the fluidized state gave way to new structure and dynamics. Actin filaments formed bundles, which in turn started connecting to each other, forming a percolated network interspersed with open regions (Fig. 2a,b, Supplementary Video 2). The emergence of

the heterogeneous network of bundles was reflected in an increasing variance of actin density, which coincided with sheet formation (Fig.2b, II). This structural transformation was accompanied by changing dynamics. Both MT and actin speeds decreased (Fig.2c, II), while their velocity fields decorrelated from each other (Fig.2d, II), suggesting formation of an actin elastic network that increasingly resisted active flows.

As a connected sheet of actin bundles formed, the MT bundles moved through and interacted with this porous and elastic network (Supplementary Video 3). To quantify the coupling between the active fluid and passive sheet, we segmented the image into regions interior and exterior to the sheet and computed quasi-2D flow fields of interior and exterior MTs (Fig.2c, inset). The interior MTs moved slightly faster than the sheet itself, but the two speeds were highly correlated. In comparison, exterior MTs were largely uncorrelated with the sheet and moved about twice as fast (Fig.2c and d,II).

By ~ 7.5 hours, the actin network reached a structural steady state in terms of network heterogeneity and sheet thickness (Fig.2b, III). The spatially-averaged speed of in-plane sheet deformations fluctuated around a constant value (Fig. 2c, III), and the cross-correlation between between MT and actin velocities remained constant (Fig. 2d, III). The actin sheet, however, gradually developed new dynamical features, as reflected in temporal oscillations of the mean speed (Fig.2c,III). The system thus undergoes three stages of self-organized dynamics: (I) initial fluidized dynamics, (II) network assembly, elasticity buildup, and sheet contraction, and (III) activity-driven sheet deformations.

To understand how the active fluid drives the actin sheet, we compared the length and time scales of their velocity fields during hours 4-7 after sample activation, corresponding to a slowly contracting yet essentially fully-formed actin network. We characterized the elastic deformations of the actin sheet by its velocity field spatial autocorrelation, which decayed exponentially with a length scale of $127 \mu\text{m}$. These deformations were driven by extensile MT bundles, which were found both inside and outside the sheet. Compared to the sheet, the flows of the exterior MTs were correlated on a much shorter length scale of $26 \mu\text{m}$ (Fig.2e). The flow field of interior MTs exhibited two exponential regimes, with lengthscales of $\sim 30 \mu\text{m}$ and $\sim 130 \mu\text{m}$ respectively, and a crossover at $\sim 50 \mu\text{m}$. The flow on short length scales of both the exterior and interior MTs was comparable to that previously observed [10], while the persistent correlation at long length scales exhibited by the interior MTs reflects coupling to the elastic sheet. The temporal velocity autocorrelation of exterior MTs decayed exponentially with a timescale of ~ 5 min (Fig.2f). In contrast, the velocity field of interior MTs was anti-correlated for time lags of ~ 5 -20 min, indicating that the active fluid consistently reversed its direction of motion on this time scale. This flow anti-correlation was more pronounced in the velocity temporal autocorrelation of the actin sheet, which could

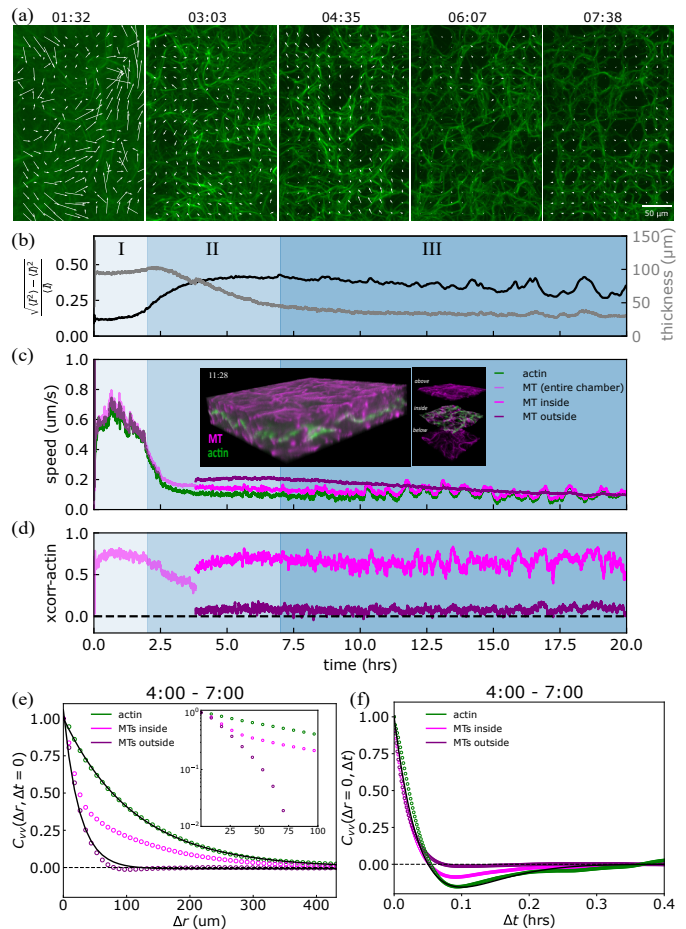


FIG. 2. Temporal evolution of the elastic sheet (a) Actin sheet imaged over time. Arrows indicate the decreasing magnitude of the actin velocity field. Images are 2D maximum-intensity z-projections of 3D confocal images. The timestamp is hh:mm. (b) The mean thickness of the actin sheet, obtained from image segmentation is shown in black. The ratio of standard deviation to mean of the actin fluorescence intensity, computed from 2D projections. $\sigma \equiv \sqrt{\langle I^2 \rangle - \langle I \rangle^2} / \langle I \rangle$. Shaded regions indicate three stages of the sample evolution: (I) network formation, (II) Emergence of the elastic sheet (III) Steady-state dynamics (c) Mean speed of MTs and actin over time. Inset: Segmentation used for projections at 3.8 hours. (d) Cross-correlation of actin and MT velocity fields. Legend for MT populations is the same as that in (c). (e) Velocity spatial autocorrelations of the actin sheet and interior and exterior MTs. The solid lines are exponential fits. Inset: Autocorrelations plotted on a semi-log plot. (f) Velocity temporal autocorrelations. The solid line is a fit to the damped harmonic oscillator.

be fit to the functional form of a 1D damped harmonic oscillator. Taken together, these observations suggest that the short-range flows of active MT bundles drive deformations of the actin sheet that persist over large length and time scales and are imprinted back onto the motion of the interior MTs.

IV. TRANSITION FROM STRETCHING TO BENDING DYNAMICS

Next, we investigated the activity-driven deformations of an elastic sheet using principles of plate elasticity. We studied a sample whose composition ensured that actin was bundled before activation. Therefore, upon activation, actin bundles rapidly formed a connected elastic sheet whose thickness contracted quickly, stabilizing at $\sim 50 \mu\text{m}$ for several hours before contracting further (Fig. 3c). The elastic sheet also exhibited increasingly more pronounced in-plane and out-of-plane deformations. The unique features of our system allowed us to measure both the height deformations and in-plane strains as the evolving elastic sheet was being sculpted and driven by active fluids (Fig. 3a,b).

To understand the relationship between the sheet's deformations and its thickness, we note that the strain tensor of an elastic sheet, defined at each point in the x - y plane, is given by $\epsilon_{ij} = u_{ij} + \frac{1}{2}\partial_i h \partial_j h$, where $u_{ij} = \frac{1}{2}(\partial_i u_j + \partial_j u_i)$ are the 2D in-plane strains, u_i are the 2D in-plane components of the displacement, and h is the local height of the membrane mid-surface [18]. For an elastic sheet with thickness t , the bending modulus scales as t^3 while the stretching modulus scales as t . Decreasing thickness thus favors bending deformations. This generates low energy modes where the bending contribution to the strain tensor, $\frac{1}{2}\partial_i h \partial_j h$, is compensated by the in-plane contribution u_{ij} to keep the 3D strain tensor ϵ_{ij} and associated stretching energy small. These bending modes (or flexural phonons) have been shown to renormalize the effective bending stiffness of thermally equilibrated thin membranes such as the isolated spectrin cytoskeleton of red blood cells and even atomically thin metamaterials such as graphene [19, 20].

In our experiment, the actin sheet underwent rapid contraction in thickness, reaching a plateau of $\sim 50 \mu\text{m}$ between hours 1-4, during which it underwent 2D compression in the x - y plane (Fig. 3d). The in-plane strains were large, while the height gradients were negligible. Subsequently, as the sheet gradually contracted further to $\sim 10 \mu\text{m}$, the height gradients increased dramatically, approaching the in-plane strains in magnitude. Further compaction at long times allows the sheet to transfer its in-plane deformation to low-energy bending degrees of freedom. Such dynamics greatly depend on the rate at which the sheet reaches its steady-state thickness. Sheets can also compact rapidly to $\sim 5 \mu\text{m}$ thickness. In this scenario, the out-of-plane bending and in-plane stretching reached comparable magnitudes almost immediately (Fig. S1). The bending and in-plane stretching components of the strain tensor ϵ_{ij} canceled each other quantitatively, demonstrating that the non-equilibrium dynamics of thin actin membranes are driven by pure bending modes.

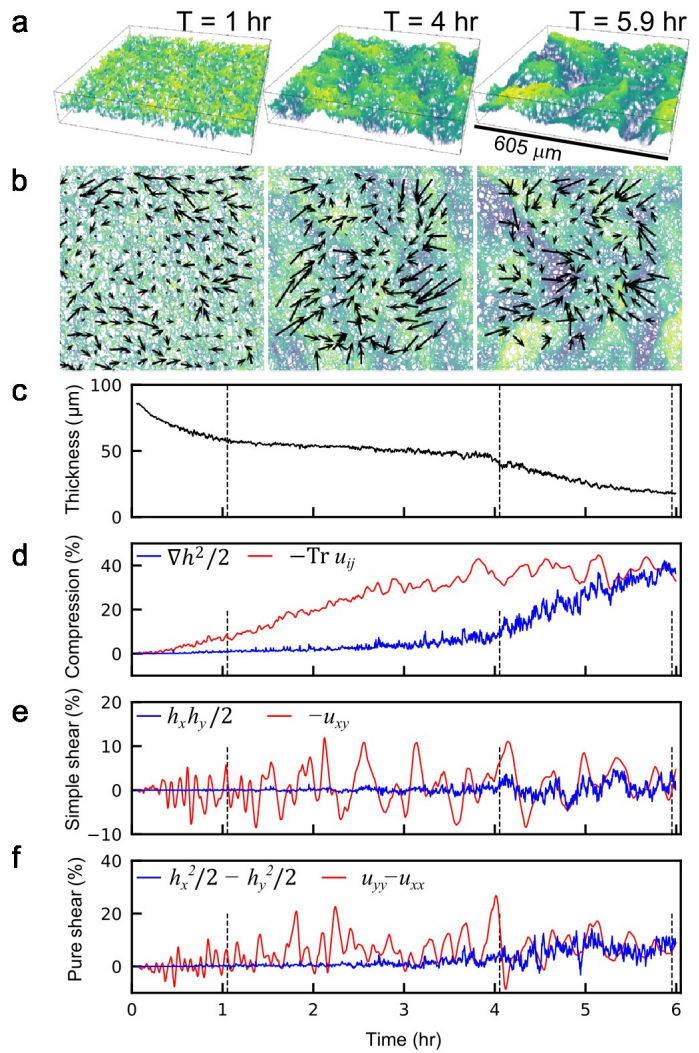


FIG. 3. **Transition from stretching to bending dynamics** (a) 3D projections of membrane structure at three time points during the evolution of an active membrane for a sample with $4 \mu\text{m}$ actin. The membrane develops local out-of-plane bends as it compacts. Colors indicate local membrane height. A small section of the membrane is shown. (b) Relative in-plane displacements (black arrows), defined as $\Delta u_i \equiv u_i - \langle u_i \rangle_{x,y}$, that correspond to the time points depicted above. The displacements are overlaid on 2D projections of the membrane structure. Colors indicate local membrane height. (c) Membrane thickness over time, averaged over a local field of view. Vertical dashed lines indicate the time points depicted in the above images. (d)-(f) Negative in-plane (red) and out-of-plane components (blue) of compressional strain and the two components of shear strain, averaged in a local field of view.

V. GLOBAL OSCILLATIONS

The in-plane deformations exhibit coarsening over time, leading to system-sized shear oscillations (Fig. 4a,b). At early times, the velocities are correlated over relatively short distances of $\sim 100 \mu\text{m}$ (Fig. 4b,

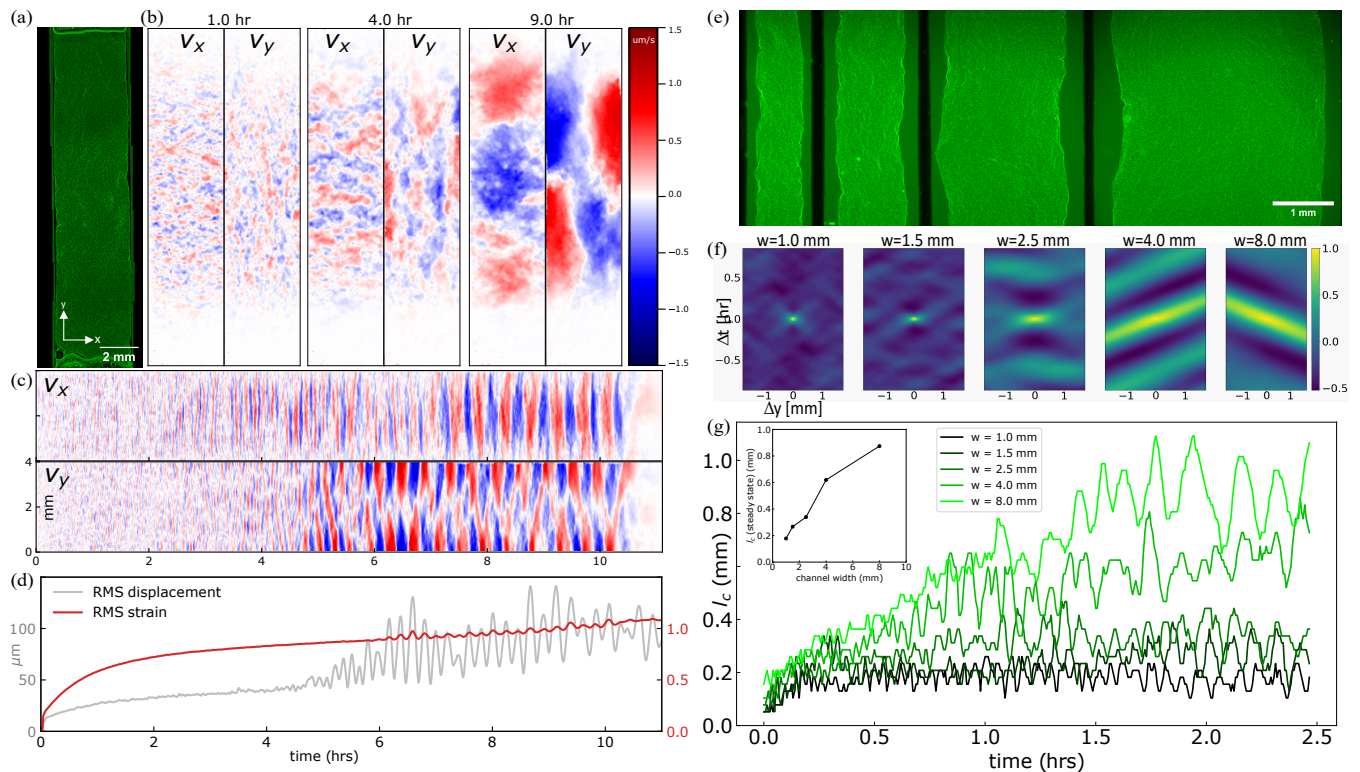


FIG. 4. **System-spanning oscillations.** (a) Image of centimeter-sized actin network. (b) Velocity field coarsens over time. (c) Kymographs of the velocity field components across a horizontal line at the center of the sample. (d) Root-mean-square displacement and strain of the actin network over time. (e) A series of experiments of identical mixture and varying channel width. Left to right: 1.0, 1.5, 2.5, 4.0 mm wide channels (8 mm wide channel not shown). (f) Spatiotemporal autocorrelations (y, t) for the different channels. (g) Velocity correlation length over time for the samples in channels of varying width. Inset: Mean steady-state correlation length as a function of channel width.

left panel). The domains of coherent motion steadily increased in size, saturating only when reaching the system size ~ 2 mm (Fig. 4b, center and right panels). At late times, the system-spanning velocity pattern comprised large-wavelength spatial modes of v_x and v_y , forming two counter-rotating vortices along the sample's length, with both switching the direction of rotation after every cycle (Supplementary Video 5). The oscillation frequency also emerged gradually from uncorrelated fluctuations (Fig. 4c). Intriguingly, the oscillatory dynamic emerged in v_y about two hours earlier than in v_x .

The oscillations in the velocity field corresponded to oscillations in the spatially averaged root-mean-square displacement (Fig. 4d). In this sample, the actin network formed quickly without an extended fluidization phase, allowing the displacement field to be computed from the onset of activity. For the first 4.5 hours, the RMS displacement increased gradually to ~ 50 μm , after which oscillations of average amplitude ~ 30 μm began to develop. This demonstrates that material points of the actin network oscillated about a reference configuration, consistent with its being a soft elastic solid.

The oscillatory dynamics were controlled by the sample geometry. We varied the sheet width, w , while keeping

the length, $l = 18$ mm, constant (Fig. 4e). The spatiotemporal velocity autocorrelations revealed distinct dynamics for different sample widths (Fig. 4f). For $w = 4$ mm, and $w = 8$ mm, the actin sheet exhibited traveling wave motion. For $w = 2.5$ mm, periodicity in time, but not in space, was observed. In narrower channels, oscillations were suppressed. In all samples, the velocity correlation length, l_c , steadily increased before fluctuating about a steady-state value, with wider systems taking a longer time to reach this state (Fig. 4g). In the steady state, $l_c \approx 0.1w$ across all samples (Fig. 4g, inset), demonstrating a strong effect of geometric confinement on the dynamics.

VI. CONTROLLING NETWORK STRUCTURE AND DYNAMICS

The structure and dynamics of actin networks were robustly controlled by the fascin concentration. We prepared a series of samples with fixed active fluid composition and actin concentration $c_a = 2.0$ μM , and varied the fascin concentration from $c_f = 0.0$ μM to 2.0 μM . Prior to the onset of activity, actin filaments were unbundled for $c_f = 0.0$ μM to 0.8 μM , with increased bundling

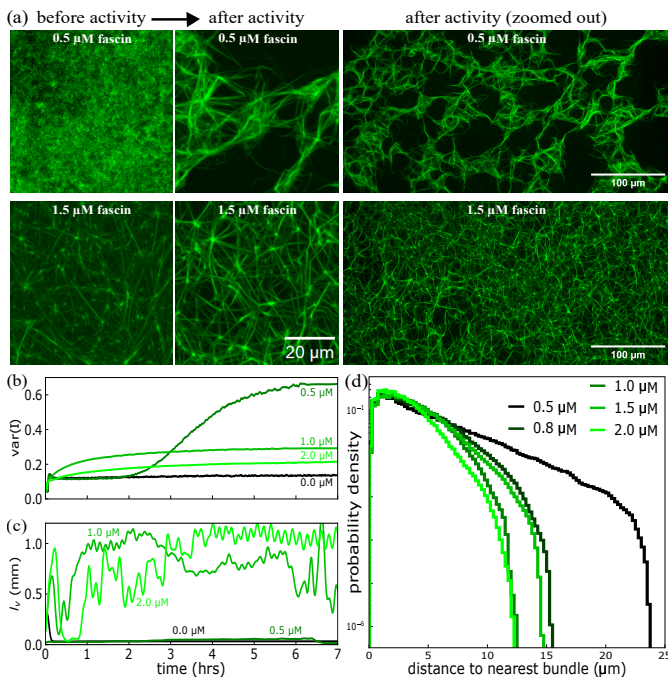


FIG. 5. **Crosslinker-dependent structure and dynamics.** (a) Snapshots of 488-phalloidin-labeled actin before and after activity, for two different fascin concentrations. All samples: 2 μM actin. (b) Normalized variance of actin fluorescence intensity. Labels indicate fascin concentration. (c) Actin velocity correlation length for different fascin concentrations. (d) Structure of the static networks after the activity has ceased.

for $c_f = 1.0 \mu\text{M}$ to $2.0 \mu\text{M}$ (Fig. 5a, left). The initial actin-fascin bundling conditions determined the subsequent evolution of the system after sample activation (Fig. 5b). In the absence of fascin, actin filaments were continuously fluidized by the chaotic active fluid, leading to low spatial variance in actin density throughout the sample lifetime. In contrast, for $c_f = 0.5 \mu\text{M}$ sample the actin density variance increased dramatically after ~ 2 hours, reflecting an initial fluidization period followed by the formation of densely bundled patches mediated by sparse open regions. When c_f was increased to $0.8 \mu\text{M}$, actin density variance increased steadily following sample activation, reflecting a very brief fluidization period before bundling and network formation. The fluidization period was absent in samples that were pre-bundled before activation ($c_f = 1.0 \mu\text{M}$ to $2.0 \mu\text{M}$), which exhibited only slight coarsening of the actin density field.

The distinct fascin-dependent structures of the emergent actin networks were accompanied by distinct dynamics. For $c_f = 0.0 \mu\text{M}$ and $0.5 \mu\text{M}$, the correlation length of the in-plane actin velocity field remained $\lesssim 100 \mu\text{m}$ for the entire lifetime, reflecting the chaotic flow of fluidized, unbundled actin filaments, or the uncorrelated motion of a sparse, floppy actin network (Fig. 5c). In contrast, samples with initially bundled actin ($c_f = 1.0, 1.5, 2.0 \mu\text{M}$) exhibited correlated flow on length scales

of $\sim 1 \text{ mm}$, corresponding to global shear oscillations that developed immediately upon sample activation (Supplementary Video 6).

Once activity was depleted, the final actin structures were distinct from the initial structures. Low-fascin networks were characterized by regions of densely tangled actin bundles and large pores nearly devoid of actin (Fig. 5a, center and right). In contrast, pre-bundled high fascin networks provided a template upon which additional filaments were attached during the active period. To quantify the network structures after activity, we computed the probability of voxels in the void being a distance r from the closest fiber (Fig. 5c). The heterogeneous low-fascin networks had a broader $\rho(r)$ distribution in comparison to high fascin concentrations. Thus, active fluid generated elastic networks with controlled structures that are not easily accessible using conventional methods.

VII. DISCUSSION

We described how layers of intervening structures and dynamics emerge from an initial structureless mixture of passive and active components. At long times these hierarchical self-organizing processes generate thin elastic sheets exhibiting global oscillations. Oscillatory dynamics might be a ubiquitous feature of active solids [21–23]. Compared to previous studies our system does not exhibit any alignment of the active agents. Previous studies on filaments and associated motors have been shown to generate diverse contractile processes, but these always lead to static structures at long time [24–29]. We showed that separating the active drive and passive stresses greatly expanded the range of accessible dynamics, generating long-term dynamical states, akin to those observed in living matter. Building on recent advances [15], our work also demonstrated how turbulent-like flows can drive the assembly of otherwise passive objects into structures and materials that cannot be obtained with conventional routes. We assemble filamentous networks, a class of materials with unique mechanical properties and transitions [30–32]. This opens up the alluring possibility of tailoring the structure of the active flows to control both the network structure and mechanics as well as patterns of in-plane strains exerted on the elastic sheets. The actin/MT composites are driven by internal feedback where activity builds structures which in turn change the patterns of active stresses and the ensuing dynamics. Understanding such processes represents not only a theoretical challenge but also a step toward creating dynamical life-like materials.

VIII. ACKNOWLEDGEMENTS

We thank Layne Frechette, Bulbul Chakraborty, and Xiaoming Mao for insightful discussions. This work was

primarily supported by the Department of Energy (DOE) DE-SC0022291. The theory was supported in part by grant NSF PHY-2309135 to the Kavli Institute for Theoretical Physics (MB).

IX. SUPPLEMENTARY INFORMATION

A. Experimental methods

Apart from the addition of the actin crosslinker fascin, the sample recipe was largely similar to the previous work [17]. Actin was purified from rabbit muscle acetone powder (Pel-Freez), incubated with the non-hydrolyzable ATP analog AMP-PNP, and diluted to final concentrations of 2-4 μM . Fascin was used at final concentrations of 2-4 μM , while phalloidin (labeled with Alexa Fluor 488 dye, Thermo Fisher) was kept constant at 670 nm across all samples. The active fluid consisted of tubulin (3% of monomers labelled with Alexa Fluor 647 dye) polymerized into microtubules (25 μM), K401-SA motor clusters (200 nm), and truncated PRC1 (400 nm). Caged ATP (2 mM) and a regeneration system of PK/LDH and PEP (20 or 40 mM) were used. We observed that high levels of PEP resulted in weaker actin-fascin bundling for the same concentrations of actin and fascin. An antioxidant mixture of glucose (2.82 mg/ml), glucose oxidase (0.22 mg/ml), glucose catalase (0.04 mg/ml), DTT (5.6 mM) were used to prevent bleaching.

Actin and fascin were mixed in a single solution and diluted in an ATP-free G-buffer (2 mM HEPES, 0.1 mM CaCl_2 , pH 7.5 with KOH). All other components were mixed in M2B buffer (80 mM PIPES, 2 mM MgCl_2 , 1 mM EGTA, pH 6.8 with KOH). Then, these two solutions were combined to form the final mixture, with an additional 10X M2B added so that the final buffer condition was approximately 1X M2B. The salt levels in the M2B/premix were sufficient to induce actin polymerization. The final mixture was loaded into chambers (acrylamide-coated coverslips, parafilm walls), sealed with 5-minute epoxy, and allowed to incubate for 1 hour at room temperature for actin to polymerize fully. Subsequently, the sample was mounted on the microscope and exposed to UV light for one minute in order to uncage the ATP.

Samples were imaged with epifluorescence microscopy, with widefield or spinning disk confocal (X-Light V2, CrestOptics). Widefield images were acquired with 4X air objective (NA=0.20). Confocal images were acquired with a sCMOS camera (Prime95B, Photometrics) and binned to obtain 804×804 squared pixels. Time series of confocal two-fluorescence-channels (647 nm for MTs, 488 nm for the fluorescent-phalloidin-labeled actin filaments) image stacks were acquired using a 20X air objective (NA=0.75). Data in Fig. 2 was acquired with a 2.2 μm z-step and a 5.5 s time interval between stacks. Data in Fig. 3 was acquired with a 2.5 μm z-step and a 11.0 s time interval. Static images of actin filaments/bundles before

and after activity (Fig. 5) were acquired with a 40X water immersion objective (NA=1.15) and 0.55 μm z-step.

B. Analysis methods

Rendering of 3D composite system (Fig. 1): The 3D image of the two fluorescent channels (488 nm for phalloidin-labeled actin, 647 nm for microtubules) was rendered using Imaris software.

In-plane velocities from confocal data (Figs. 2, 3, S1): To adjust uneven brightness over the field of view, images were divided by a background image. Each confocal z-stack in the time sequence was converted to a 2D image using maximum-intensity z-projection. Instantaneous in-plane velocity fields were estimated using Particle Image Velocimetry (PIV) software [33].

In-plane velocities from wide-field data (Figs. 4): Instantaneous in-plane velocity fields were estimated using PIV [33]. Masks were used to account for the membrane boundaries. For the 8 mm wide samples, two images were stitched to visualize the entire membrane width.

Calculation of velocity autocorrelations (Figs. 2 and 4): We calculated the scalar autocorrelation of the velocity field $C_v(\Delta x, \Delta y, t) = \langle \vec{v}(x + \Delta x, y + \Delta y, t + \Delta t) \cdot \vec{v}(x, y, t) \rangle$ using a Fast Fourier Transform. To avoid circular autocorrelation, the velocity fields were zero-padded by 1/4th of the field size on both side of the x - and y -axes. The padded field was convolved with a copy of it with axes reversed using the function `fftconvolve` of the SciPy package with a ‘valid’ mode setting. Correlation values were locally normalized to take into account the change of correlation window size at the field boundaries due to the padding.

Calculation of in-plane displacements (Figs. 2, 3, S1): In-plane displacements were calculated from the in-plane velocity fields using an modified MATLAB function (TecPIV) [34]. Briefly, a time point was chosen to serve as the material frame of reference $\vec{X}(t = 0) = (x_0, y_0)$. Points of the material frame were propagated with the local velocities to obtain the displacements $\vec{u}(x_0, y_0) = \vec{v}(x_0, y_0)\Delta t$. The position of the material points was calculated $\vec{X}(t = \Delta t) = \vec{X}(t = 0) + \vec{u}$. To calculate the displacement at the next time point, velocities were interpolated at the propagated material points, and the incremental displacements were added to the displacement of the previous time point. This process was repeated to obtain the displacements for the entire time sequence. Because the membrane exhibited large displacements, material points that exited the field of view were subsequently eliminated from further propagation.

Detection of membrane mid-plane, normals and thickness (Fig. 2): To adjust uneven brightness over the field of view, images were divided by a background image. Binary masks were created at each time point by hysteresis thresholding the preprocessed stacks (low and high thresholds above the background intensity level: 30% and 50% respectively). Masked stacks were coarse-

grained recursively. Each stack was fitted to a plane, by computing its 3D center of mass and its 2nd moment principal axes. A stack was deemed ‘planar’ if the shortest axis was at least twice shorter than the next longest axis. Then, the stack was divided into 4 equal-size substacks along the xy plane, and the planar fitting was repeated for each substack. If a substack was ‘planar’ and the average of the residuals of the newly fitted plane were smaller by at least 3 standard deviations from the parent stack, the substack was divided into 4 and the process was repeated, otherwise it was stopped. The center-of-mass, normal and residual sum were collected for each substack at which the subdivision stopped. The local thickness was defined to be 4 times the average of the residuals (2 standard deviations). The result of this algorithm is a collection of center-of-mass points and normal vectors that define the mid plane of the membrane, as well as the local membrane thickness at each center-of-mass point. To convert the thickness to physical units, the z-step of microscope stage movement was multiplied by a correction factor of 1.33 to account for the refractive index mismatch between the sample (water) and the intervening medium (air).

Calculation of in-plane and out-of-plane strains from confocal data (Figs. 3 and S1): The in-plane strains $u_{ij} = (u_i + u_j)/2$ were computed from the in-plane displacement fields using Gaussian smooth derivatives with σ that equaled the PIV step size. The strains were decomposed into their compression $-(u_{xx} + u_{yy})$, simple shear u_{xy} and pure shear $u_{yy} - u_{xx}$ components. The out-of-plane strain components were estimated from the normal vector field $\hat{\mathbf{n}} = (\hat{n}_x, \hat{n}_y, \hat{n}_z)$ via the approximated formulas $h_x \simeq -\hat{n}_x(1 + (\hat{n}_x^2 + \hat{n}_y^2)/2)$, $h_y \simeq -\hat{n}_y(1 + (\hat{n}_x^2 + \hat{n}_y^2)/2)$, where h_x and h_y are the partial derivatives of the membrane height along the x and the y axes respectively.

Characterization actin network structure (Fig. 5d): For characterizing the network structure from 40X WI confocal z-stacks, the actin fluorescence images were segmented using a custom training routine in the ‘‘ilastik’’ software [35]. Subsequently, the probability maps were binarized, and the binary images were skeletonized. Then, a 3D distance transform (SciPy) was computed.

C. Supplementary Videos

Supplementary Video 1: Timelapse of rendered 3D confocal image sequence of fluorescent actin and fascin.

Supplementary Video 2: Timelapse of projected 3D confocal images showing actin filaments form bundle network over time.

Supplementary Video 3: Simultaneous timelapses of actin and MTs inside, above, and below the actin network.

Supplementary Video 4: Bending and stretching dynamics of actin sheet.

Supplementary Video 5: Widefield tiled video of

actin network developing oscillations, along with heat maps of v_x and v_y components.

Supplementary Video 6: Widefield timelapse of samples with varying fascin, showing the transition from floppy to oscillatory dynamics.

D. Supplementary Figures

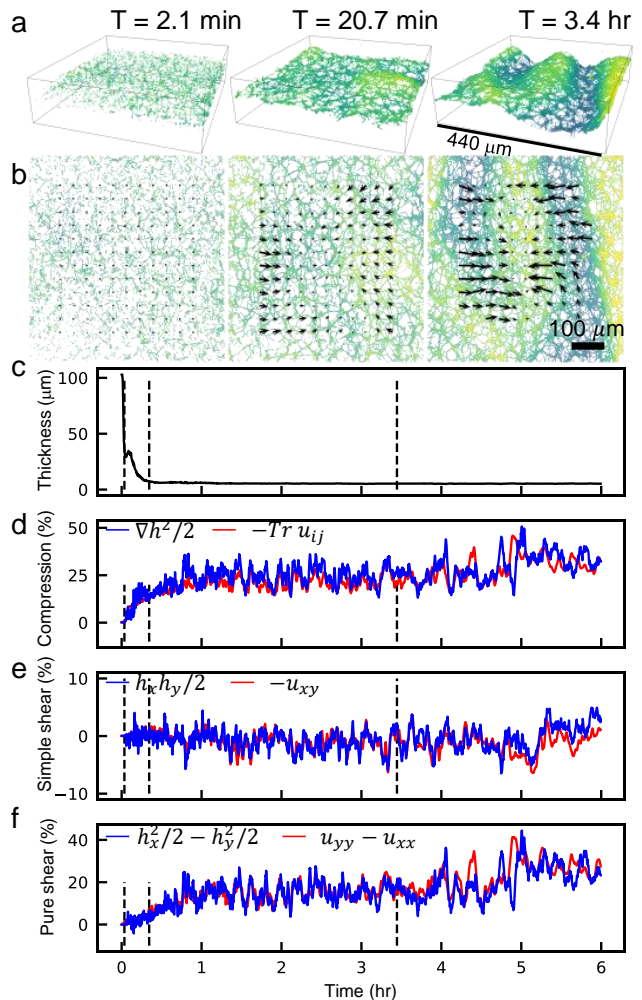


FIG. S1. **Deformations of a thin actin sheet.** Similar to Fig 3 but for a membrane that compacts more rapidly. (a) 3D projections of membrane structure over time. Color indicates membrane height. (b) Relative in-plane displacements (black arrows), defined as $\Delta u_i \equiv u_i - \langle u_i \rangle_{x,y}$, that correspond to the time points depicted above. (c) Membrane thickness over time, averaged over a local field of view. Vertical dashed lines indicate the time points depicted in the above images. (d)-(f) Negative in-plane (red) and out-of-plane components (blue) of compressional strain and the two components of shear strain, averaged in a local field of view. Images taken with a 40X water immersion objective. 12.4 s time interval. 1 μm z-step. PIV parameters: PIV step, 28.6 μm.

- [1] A. C. Martin, M. Kaschube, and E. F. Wieschaus, Pulsed contractions of an actin–myosin network drive apical constriction, *Nature* **457**, 495–499 (2008).
- [2] N. P. Mitchell, D. J. Cislo, S. Shankar, Y. Lin, B. I. Shraiman, and S. J. Streichan, Visceral organ morphogenesis via calcium-patterned muscle constrictions, *Elife* **11**, e77355 (2022).
- [3] D. Nykypanchuk, M. M. Maye, D. van der Lelie, and O. Gang, Dna-guided crystallization of colloidal nanoparticles, *Nature* **451**, 549–552 (2008).
- [4] S. M. Douglas, H. Dietz, T. Liedl, B. Högberg, F. Graf, and W. M. Shih, Self-assembly of dna into nanoscale three-dimensional shapes, *Nature* **459**, 414–418 (2009).
- [5] W. M. Jacobs, A. Reinhardt, and D. Frenkel, Rational design of self-assembly pathways for complex multicomponent structures, *Proceedings of the National Academy of Sciences* **112**, 6313–6318 (2015).
- [6] M. He, J. P. Gales, E. Ducrot, Z. Gong, G.-R. Yi, S. Sacanna, and D. J. Pine, Colloidal diamond, *Nature* **585**, 524–529 (2020).
- [7] W.-S. Wei, A. Trubiano, C. Sigl, S. Paquay, H. Dietz, M. F. Hagan, and S. Fraden, Hierarchical assembly is more robust than egalitarian assembly in synthetic capsids, *Proceedings of the National Academy of Sciences* **121**, e2312775121 (2024).
- [8] S. Whitelam and R. L. Jack, The statistical mechanics of dynamic pathways to self-assembly, *Annual review of physical chemistry* **66**, 143 (2015).
- [9] R. Aditi Simha and S. Ramaswamy, Hydrodynamic fluctuations and instabilities in ordered suspensions of self-propelled particles, *Physical Review Letters* **89**, 10.1103/physrevlett.89.058101 (2002).
- [10] T. Sanchez, D. T. Chen, S. J. DeCamp, M. Heymann, and Z. Dogic, Spontaneous motion in hierarchically assembled active matter, *Nature* **491**, 431 (2012).
- [11] H. H. Wensink, J. Dunkel, S. Heidenreich, K. Drescher, R. E. Goldstein, H. Löwen, and J. M. Yeomans, Mesoscale turbulence in living fluids, *Proceedings of the national academy of sciences* **109**, 14308 (2012).
- [12] S. Zhou, A. Sokolov, O. D. Lavrentovich, and I. S. Aranson, Living liquid crystals, *Proceedings of the National Academy of Sciences* **111**, 1265–1270 (2014).
- [13] X.-L. Wu and A. Libchaber, Particle diffusion in a quasi-two-dimensional bacterial bath, *Physical Review Letters* **84**, 3017–3020 (2000).
- [14] D. Mizuno, C. Tardin, C. F. Schmidt, and F. C. MacKintosh, Nonequilibrium mechanics of active cytoskeletal networks, *Science* **315**, 370 (2007).
- [15] D. Grober, I. Palaia, M. C. Uçar, E. Hannezo, A. Šarić, and J. Palacci, Unconventional colloidal aggregation in chiral bacterial baths, *Nature Physics* **19**, 1680–1688 (2023).
- [16] O. Lieleg, M. M. A. E. Claessens, C. Heussinger, E. Frey, and A. R. Bausch, Mechanics of bundled semiflexible polymer networks, *Phys. Rev. Lett.* **99**, 088102 (2007).
- [17] J. Berezney, B. L. Goode, S. Fraden, and Z. Dogic, Extensible to contractile transition in active microtubule–actin composites generates layered asters with programmable lifetimes, *Proceedings of the National Academy of Sciences* **119**, 10.1073/pnas.2115895119 (2022).
- [18] L. D. Landau, L. P. Pitaevskii, E. M. Lifshitz, and A. M. Kosevich, *Theory of Elasticity* (1986).
- [19] D. Nelson and L. Peliti, Fluctuations in membranes with crystalline and hexatic order, *Journal de physique* **48**, 1085 (1987).
- [20] M. K. Bles, A. W. Barnard, P. A. Rose, S. P. Roberts, K. L. McGill, P. Y. Huang, A. R. Ruyack, J. W. Kevek, B. Kobrin, D. A. Muller, and P. L. McEuen, Graphene kirigami, *Nature* **524**, 204–207 (2015).
- [21] E. Hemingway, A. Maitra, S. Banerjee, M. Marchetti, S. Ramaswamy, S. Fielding, and M. Cates, Active viscoelastic matter: From bacterial drag reduction to turbulent solids, *Physical Review Letters* **114**, 10.1103/physrevlett.114.098302 (2015).
- [22] S. Liu, S. Shankar, M. C. Marchetti, and Y. Wu, Viscoelastic control of spatiotemporal order in bacterial active matter, *Nature* **590**, 80–84 (2021).
- [23] P. Baconnier, D. Shohat, C. H. López, C. Coulais, V. Démery, G. Düring, and O. Dauchot, Selective and collective actuation in active solids, *Nature Physics* **18**, 1234–1239 (2022).
- [24] S. Köhler, V. Schaller, and A. R. Bausch, Structure formation in active networks, *Nature materials* **10**, 462 (2011).
- [25] M. P. Murrell and M. L. Gardel, F-actin buckling coordinates contractility and severing in a biomimetic actomyosin cortex, *Proceedings of the National Academy of Sciences* **109**, 20820–20825 (2012).
- [26] J. Alvarado, M. Sheinman, A. Sharma, F. C. MacKintosh, and G. H. Koenderink, Molecular motors robustly drive active gels to a critically connected state, *Nature Physics* **9**, 591–597 (2013).
- [27] P. J. Foster, S. Fürthauer, M. J. Shelley, and D. J. Needleman, Active contraction of microtubule networks, *Elife* **4**, e10837 (2015).
- [28] G. Livne, S. Gat, S. Armon, and A. Bernheim-Groswasser, Self-assembled active actomyosin gels spontaneously curve and wrinkle similar to biological cells and tissues, *Proceedings of the National Academy of Sciences* **121**, 10.1073/pnas.2309125121 (2024).
- [29] G. Lee, G. Leech, M. J. Rust, M. Das, R. J. McGorty, J. L. Ross, and R. M. Robertson-Anderson, Myosin-driven actin-microtubule networks exhibit self-organized contractile dynamics, *Science Advances* **7**, 10.1126/sciadv.abe4334 (2021).
- [30] C. P. Broedersz, X. Mao, T. C. Lubensky, and F. C. MacKintosh, Criticality and isostaticity in fibre networks, *Nature Physics* **7**, 983–988 (2011).
- [31] A. Sharma, A. J. Licup, K. A. Jansen, R. Rens, M. Sheinman, G. H. Koenderink, and F. C. MacKintosh, Strain-controlled criticality governs the nonlinear mechanics of fibre networks, *Nature Physics* **12**, 584–587 (2016).
- [32] M. Bantawa, B. Keshavarz, M. Geri, M. Bouzid, T. Divoux, G. H. McKinley, and E. Del Gado, The hidden hierarchical nature of soft particulate gels, *Nature Physics* **19**, 1178–1184 (2023).
- [33] W. Thielicke and R. Sonntag, Particle image velocimetry for matlab: Accuracy and enhanced algorithms in pivlab, *Journal of Open Research Software* **9**, 12 (2021).
- [34] D. Boutelier, Tecpiv—a matlab-based application for piv-analysis of experimental tectonics, *Computers and Geosciences* **89**, 186–199 (2016).

- [35] S. Berg, D. Kutra, T. Kroeger, C. N. Straehle, B. X. Kausler, C. Haubold, M. Schiegg, J. Ales, T. Beier, M. Rudy, K. Eren, J. I. Cervantes, B. Xu, F. Beuttenmueller, A. Wolny, C. Zhang, U. Koethe, F. A. Hamprecht, and A. Kreshuk, ilastik: interactive machine learning for (bio)image analysis, *Nature Methods* **16**, 1226–1232 (2019).